Icarus 225 (2013) 15–27

Contents lists available at SciVerse ScienceDirect

Icarus

journal homepage: www.elsevier.com/locate/icarus

Layered convection in Io: Implications for short-wavelength surface topography and heat flow

M.H. Shahnas [a,*], R.N. Pysklywec [b], W.R. Peltier [a]

[a] Department of Physics, University of Toronto, 60 St. George Street, Toronto, Ontario, Canada M5S 1A7
[b] Department of Earth Sciences, University of Toronto, 22 Russell Street, Toronto, Ontario, Canada M5S 3B1

ARTICLE INFO

Article history:
Received 17 December 2011
Revised 26 February 2013
Accepted 10 March 2013
Available online 2 April 2013

Keyword:
Io
Interiors
Planetary dynamics
Geological processes
Tectonics

ABSTRACT

Io, one of the four Galilean moons of Jupiter is remarkable for its extensive volcanism and extreme interior tidal heating. The tidal heating likely yields a very low viscosity asthenosphere and consequently a very high Rayleigh number of $O(10^{12})$ for convection in the interior. In a state of quasi-steady balance the internally generated heat must be transported from the interior to the base of the Io lithosphere and exhausted to space. The mechanisms whereby the convective radial heat transfer is evacuated involve both conduction and volcanism. Despite Io's ubiquitous volcanism, only 4% of its mountains (montes) appear to have a volcanic origin and most of the mountainous regions seem to be related to tectonic processes. By employing an original control volume based numerical model we investigate the style of convection in the interior of Io and the correlation of the scale of convection with the Ionian surface heat flux and topography. Our control volume results support the existence of significant asthenospheric heating and demonstrate that short wavelength features of the surface heat flux are well correlated in scale to an expected layered intra-lithospheric style small-scale convection. These numerical analyses suggest that the amplitude of the short wavelength topography of Io is expected to be on the order of a few hundreds of meters. The model results also demonstrate that the Ionian highs cannot be produced by a lithospheric flexure process above the hot upwellings and therefore other tectonic events, such as have previously been suggested; must be responsible for the formation of the high Ionian mountains that reach in excess of 17 km in elevation.

1. Introduction

Among the 64 confirmed moons of Jupiter, Io is one of the four largest of the innermost Galilean group (along with Europa, Ganymede, and Callisto) and is remarkable because of its intensive volcanic activity. The Voyager spacecraft provided the first direct observations of this activity (Spencer and Schneider, 1996; McEwen et al., 1998a,b). The surface of Io is marked by signatures of widespread volcanic resurfacing in the recent geologic past. More specific observations in the visible and near infrared portions of the electromagnetic spectrum have revealed the existence of volcanic plumes and lava flows reaching temperatures of approximately 1800 K (McEwen et al., 1998b; Lopes-Gautier et al., 1999). The high-temperature lavas suggest a predominantly silicate character of Io volcanism (McEwen et al., 1998a,b).

Despite Io's pervasive volcanism, only 4% of the Ionian regions of high topographic relief are volcanic in origin. From 96 selected Ionian mountains (out of 143) for which sufficiently high resolution imaging exists, three seem to be volcanic, 92 appear to be edifices constructed by other tectonic events (Jaeger et al., 2003) and one is ambiguous. Io is found to be a triaxial ellipsoid in shape with major, intermediate and minor radii respectively $a = 1830.0$ km, $b = 1818.7$ km, and $c = 1815.3$ km. The Ionian surface topography is defined in terms of deviations from the surface of this ellipsoid that minimize the variance in elevation differences (Ross et al., 1990). The long wavelength component of topography of Io, defined in these terms, consists of four alternating high and low regions near the equator, spaced roughly equidistant in longitude (Gaskell et al., 1988). The maximum amplitude of this long wavelength equatorial topography is approximately 1.1 km (Ross et al., 1990). The north and south poles are moderately high (0.9 km) and low (−0.3 km) in elevation respectively (Ross et al., 1990). Although the process by which the Ionian topographic highs have formed is not well understood, the mountains are expected to have been initiated tectonically, although the precise mechanism is uncertain (Turtle et al., 2001; Jaeger et al., 2003). The tectonic features are obscured by lava flows and sulfurous plume deposits which rapidly (~1 cm/yr on average) resurface its lithosphere (Johnson et al., 1979; Blaney et al., 1995; Phillips, 2000). One possibility for the initiation of mountain formation might be in

* Corresponding author. Fax: +1 416 978 8905.
E-mail addresses: shahnas@atmosp.physics.utoronto.ca (M.H. Shahnas), russ@es.utoronto.ca (R.N. Pysklywec), peltier@atmosp.physics.utoronto.ca (W.R. Peltier).

0019-1035/$ - see front matter © 2013 Elsevier Inc. All rights reserved.
http://dx.doi.org/10.1016/j.icarus.2013.03.014

response to the global compression caused by the high rate of global subsidence associated with this high rate of resurfacing (Turtle et al., 2001). The cold crust is deflected downward by the load associated with the volcanic resurfacing, causing shortening and isostatic compensation and uplift (Schenk and Bulmer, 1998). The observed mountain elevations could conceivably be explained by lithosphere thicknesses ranging from 13 km to 80 km (Jaeger et al., 2003). Since the lithosphere is generally under compression, the magma is expected to ascend along tectonic faults, thereby relieving the compression (Keszthelyi et al., 2004; Jaeger et al., 2003).

Io apparently has a differentiated iron core, the existence of which can be inferred on the basis of the oxidized nature of volcanic gases, indicating the absence of metallic iron in its silicate mantle. Metallic iron and FeS on Io are predominantly concentrated in the large Ionian core ($R_{core} \sim R_{surf}/2$) discovered by the observations made by the Galileo spacecraft (Anderson et al., 1996). This is in agreement with multi-layer models of the planetary structure based on data obtained on the basis of satellite gravity surveying (Kuskov and Kronrod, 2000). Using these gravity data Anderson et al. (2001) developed two models for Io's core, one involving pure iron and the other having an Fe–FeS eutectic composition. In the latter case, the expected average density and radius of Io's core are approximately 5150 kg/m^3 and 900 km, respectively. Similar models were constructed by Zhang and Zhang (2001); these authors found that J_2 and $\delta J_2 = J_2 - J_2^o$ are of the same order of magnitude, suggesting Io to be strongly affected by tides and that it may have a large core. Using the Galileo magnetometer data Kivelson et al. (2002) showed that Io has no significant intrinsic magnetic field. They interpret this as indicating that the core of Io is either completely solid or completely liquid. It is still unclear, however, that the existence of a solid inner core is required for a dynamo mechanism to operate. Since the Fe–FeS eutectic composition has a relatively low melting temperature (<1700 K at the pressure at Io's CMB), it is more likely that the core is completely liquid (Keszthelyi et al., 2003). Owing to the significant level of volcanic activity on Io (e.g. Spohn, 1997), the body likely has been differentiated into low-density, high-silica materials, such as potassium and sodium silicates in the crust and higher-density, lower-silica content materials in the mantle (Keszthelyi and McEwen, 1997).

Io is the most volcanically active body in our Solar System (Lopes-Gautier et al., 1999) and the activation mechanism for volcanism is quite different from that for the Earth. For the Earth, volcanic activity is powered significantly by accretion-induced heat from the early era of planet formation and radiogenic decay. However, Io is too small (less than 1/3 the radius of Earth) to be influenced significantly by remaining of accretionary heat and the radioactive sources could not provide sufficient heat to account for the prodigious power required to support the observed volcanic activity. Based on the infrared observations (Veeder et al., 1994) and estimates of tidal dissipation, the average heat flux at Io's surface may be as high as 2.5 W/m^2. This observed surface heat flow is too large to be explained by thermal conduction through a conductive lithosphere, as on the Earth, if similar thermal properties to those of the Earth's lithosphere are assumed. The heat evacuated by a conductive lithosphere alone requires a thermal gradient larger than 750 K/km. This in turn results in a very thin lithosphere ($\sim$2 km) which is inconsistent with the observed topography on Io with mountains having relief in excess of 10 km (Monnereau and Dubuffet, 2002). O'Reilly and Davies (1981) proposed that the heat is mainly advected by magma through isolated vents, rising from depth and spreading out at the surface, which supports the existence of a thick and cool Ionian lithosphere. Following the subsequent subsidence of the rigid lithosphere under the weight of evacuated flows its base is heated to the melting point. In this model the heat is mainly evacuated by advection. Based on this hypothesis and using spherical models of mantle convection, Monnereau and Dubuffet (2002) showed that the volcanism would be an efficient means by which to evacuate the heat from the interior, but at the same time allow for the maintenance of a thick rigid lithosphere. Magma may be evacuated by eruption to the surface (Carr, 1986) or be localized near the surface to drive evaporating sulfur lakes (Lunine and Stevenson, 1985). The color images provided by Voyager and the temperature estimates from the Infrared Radiometer Interferometer and Spectrometer (IRIS) instrument suggested the possibility of sulfur volcanism (Sinton, 1982). For some time it was generally accepted that sulfur volcanism was the dominant mode of eruption driven by silicate magmas (Keszthelyi et al., 2004; Smith et al., 1979). Later ground-based infrared emission observations revealed that the temperatures exceed the boiling point of sulfur in some locations (Veeder et al., 1994). Currently it is accepted that both silicate and sulfur volcanism are expected to be observed on Io's surface (Spencer and Schneider, 1996).

The first generation of thermal models for Io assumed a completely molten interior (Peale et al., 1979) in which the tidal heating was associated with lithospheric flexure. However, this is in contradiction with the observed topography (Schenk et al., 2001) and lithospheric structure (O'Reilly and Davies, 1981). Some theoretical studies suggest melt fractions less than 20% to remove heat from the mantle by melt segregation (Moore, 2001). However, the very high temperatures and orthopyroxene-rich compositions of Io's lavas based on Galileo SSI and NIMS data (McEwen et al., 1998b; Davies et al., 2001; Geissler et al., 1999) are more consistent with large degrees of partial melting within the mantle (Keszthelyi et al., 1999). Using numerical models and taking into account a "heat pipe" cooling mechanism, Monnereau and Dubuffet (2002) showed that the enormous tidal heat dissipated in Io's mantle could be evacuated efficiently by volcanism. They showed that the mantle temperature would vary as $Ra^{-1/2}$ and remain below the melting point of rocks in most of the mantle except for the regions close to the core–mantle boundary and inside upwellings which supports the existence of a thick rigid mantle consistent with the topographic features observed on Io.

It is now commonly accepted that the volcanic activity of Io originates from tidal dissipation in its interior. The heat is generated by the stresses in the interior caused by the gravitational attraction of Jupiter, coupled with the gravitational pull of Io's neighboring moons-Europa, Callisto, and Ganymede (Yoder and Peale, 1981; Ross and Schubert, 1985,1986; Segatz and Spohn, 1988). There exists a slight eccentricity in Io's orbit (Lieske, 1980), which is due to the orbital resonance with Europa and Ganymede which is referred to as a "Laplace resonance". This eccentricity causes the tide-raising potential of Jupiter on the surface of Io to oscillate. The tidal effects at Io's surface could cause a rise and fall of approximately 100 m which is more than five times in excess of the highest ocean tides on Earth. The distribution of tidal dissipation depends on the internal structure of Io. Based on this internal structure, thermal evolution and tidal heating (Schubert et al., 1981, 1986; Cassen et al., 1982; Nash et al., 1986; Ross and Schubert, 1985, 1986; Segatz et al., 1988; Fischer and Spohn, 1990) two end member models have been developed (Ross and Schubert, 1985): a deep mantle heating model with an elastic lithosphere and an asthenosphere heating model. In the first model, most of the tidal dissipation occurs deep in the mantle near the core–mantle boundary and the local partial melt in rising plumes explains the volcanic activity. In the second model, originally proposed by Schubert et al. (1981), most of the tidal heating occurs in the asthenosphere by the tidally forced circulation in this layer (Ross and Schubert, 1985). The viscously generated heat is then transferred to the base of the lithosphere by convection and evacuated to the surface by conduction and magma migration (Ross

and Schubert, 1985; Nash et al., 1986). In the deep mantle model the generated heat is concentrated beneath the polar region and decreases from pole to equator, while in the asthenosphere model the heat is localized in the equatorial region and decreases from equator to pole.

Using three-dimensional numerical models Tackley et al. (2001) showed that in the pure mantle heating model, the upwellings occur at the poles of Io with downwelling at the equator. However in this model the long wavelength nature of the alternating basins and swells could be explained by tidal dissipation in the Ionian asthenosphere which produces a topography anomaly in the equatorial region consistent with the observed long wavelength heat flow patterns. The long wavelength features of their model that develop at low and high Rayleigh numbers are similar, but short wave instabilities superimposed on long wave features only appear in the higher Rayleigh number models. Their numerical calculation relies on the scaling of the thermal diffusivity and the viscosity in order to substantially reduce the Rayleigh number to make the numerical calculation affordable while maintaining the correct heat flux and internal temperatures. Further to this limitation, the viscosity contrast between the mantle and asthenosphere in their models is assumed to be only a factor of 100. In their combined heating models in which the tidal heating occurs in both mantle and asthenosphere, although the structure in the pattern of the surface heat flux becomes small in scale as the Rayleigh number increases, the wavelength describing the characteristic length between the heat flux minima and maxima remains the same and unaffected by the Rayleigh number (Cases 5–8, Fig. 7, Tackley et al., 2001). This wavelength is larger than the characteristic wavelength describing the spacing between the hot spot peaks at the surface of Io (Rathbun et al., 2004).

In the present study we investigate the correlation between convection in the interior of Io and its surficial features using appropriate models of the convection process. The control volume formulation of the mantle convection process that we have developed enables us to construct models with the very large variations of viscosity that are characteristic of Io due to the extreme tidal heating in the interior. A viscosity contrast of order (10^{12}) will be assumed in these control volume based analyses, and the circulation characteristic of this high contrast regime will allow us to make closer Io surface observations than has previously been possible.

2. Numerical formulation of the problem

We model infinite Prandtl number convection in a cylindrical shell with a rigid boundary condition at the surface. The lithosphere of the jovian moon is approximated by a layer of high viscosity as described in the next section. The original convection model to be employed is based upon application of the control volume method (Patankar, 1980) to solve the basic hydrodynamic equations in cylindrical geometry. This method, originally developed by Spalding and his students (e.g., Patankar and Spalding, 1972; Patankar, 1980) for applications in engineering, has come to attract some attention in the area of planetary physics (e.g., Ogawa et al., 1991; Tackley, 1994, 1998; Ratcliff et al., 1996; Harder and Hansen, 2005; Stemmer et al., 2006; Tackley, 2008; Shahnas and Peltier, 2010) where applications have been presented in both Cartesian and spherical geometries.

The radial viscosity profile in our numerical models ranges from 10^{12} to 10^{24} Pa s. Owing to the very low viscosity of the asthenosphere and sharp viscosity gradients at the transition zones between asthenosphere and lithosphere and between asthenosphere and mantle a simple finite difference method cannot be applied. For the same reason the applicability of 3D numerical codes is also prohibitive. To overcome this problem a section of a cylindrical shell has been employed as the calculation domain in our numerical model of convection in Io. Cylindrical geometry is not afflicted by the same convergence problems as encountered in spherical geometry at the poles. Due to the small size of Io, the effect of compressibility is expected to be negligible. In the Boussinesq approximation the continuity equation, the expression for conservation of momentum in the infinite Prandtl number approximation in which the inertial terms compared to the viscous forces in the momentum equation are ignored, and the partial differential equation describing the conservation of internal energy are given respectively by:

$$\nabla \cdot \vec{V} = 0, \tag{1}$$

$$-\nabla P + \nabla \cdot \bar{\bar{\sigma}} - \rho g \,\hat{r} = 0, \tag{2}$$

$$C_P \rho_0 \frac{DT}{Dt} = \nabla \cdot (k \nabla T) + \Phi_T - \Phi_V, \tag{3}$$

where

$$\rho = \rho_0 [1 - \alpha (T - T_r)], \tag{4}$$

and

$$\bar{\bar{\sigma}} = \eta [\nabla \vec{V} + (\nabla \vec{V})^T]. \tag{5}$$

In these equations V, T, T_r, P, ρ, ρ_0, g, η, t, k, α denote the velocity, temperature, reference temperature, pressure, density, reference density, gravitational acceleration, dynamic viscosity, time, thermal conductivity and thermal expansivity. $\bar{\bar{\sigma}}$ is the simplified stress tensor for an incompressible fluid and $(\nabla V)^T$ in the last equation represents the transpose of the velocity gradient. In Eq. (3) Φ_T and Φ_V are the tidal heating rate and the rate of heat transferred to the surface by volcanism. We employ the following scheme to non-dimensionalize the governing field equations:

$$r = r' \Delta r, \quad T = T' \Delta T, \quad \eta = \eta' \eta_o, \quad k = k' k_o, \quad \rho = \rho' \rho_o, \quad C_P = C_P' C_o, \quad g = g' g_o, \quad \alpha = \alpha' \alpha_o, \quad \kappa = \kappa' \kappa_o, \quad t = t' \frac{d^2}{\kappa_o}, \quad P = P' \frac{\eta \kappa_o}{d^2}, \quad \sigma = \sigma' \frac{\eta \kappa_o}{d^2}, \tag{6}$$

in which zero subscripted quantities denote a reference value of the parameter and κ is the thermal diffusivity. As characteristic length and temperature scales we employ, respectively, $\Delta r = R_{surf} - R_{CMB}$ and $\Delta T = T_{CMB} - T_{surf}$.

The non-dimensional momentum equation is then given by:

$$-\nabla' P' + \nabla' \cdot \bar{\bar{\sigma}}' - R_o \rho' g' \,\hat{r} = 0, \tag{7}$$

where the Rayleigh number of the system is:

$$R_o = \frac{g_o \rho_o d^3}{\eta_o \kappa_o}. \tag{8}$$

Dropping the primes in order to simplify the notation then reduces Eq. (7) to:

$$-\nabla P + \nabla \cdot \bar{\bar{\sigma}} - R_o \rho g \,\hat{r} = 0. \tag{9}$$

In cylindrical coordinates the two components of the momentum equation are simply given by:

$$F_r = -\frac{\partial P}{\partial r} + \frac{1}{r}\frac{\partial}{\partial r}(r \tau_{rr}) + \frac{1}{r}\frac{\partial \tau_{r\theta}}{\partial \theta} - \frac{\tau_{\theta\theta}}{r} - R_o \rho g = 0, \tag{10}$$

$$F_\theta = -\frac{1}{r}\frac{\partial P}{\partial \theta} + \frac{1}{r^2}\frac{\partial}{\partial r}(r^2 \tau_{r\theta}) + \frac{1}{r}\frac{\partial \tau_{\theta\theta}}{\partial \theta} = 0, \tag{11}$$

where

$$\tau_{rr} = 2\eta \frac{\partial V_r}{\partial r}, \tag{12}$$

$$\tau_{\theta\theta} = 2\eta \left(\frac{V_r}{r} + \frac{1}{r} \frac{\partial V_\theta}{\partial \theta} \right), \tag{13}$$

$$\tau_{r\theta} = \tau_{\theta r} = \eta \left(r \frac{\partial}{\partial r} \left(\frac{V_\theta}{r} \right) + \frac{1}{r} \frac{\partial V_r}{\partial \theta} \right). \tag{14}$$

In the control volume formulation, the cylindrical momentum Eqs. (10) and (11) are integrated over the cylindrical volumes,

$$\Delta V = \frac{1}{2}(r_t^2 - r_b^2)(\theta_n - \theta_s), \tag{15}$$

where the subscripts n, s, b, and t denote the quantity at the north, south, bottom and top volume boundaries respectively.

The orbital period of Io is approximately 42 h, implying that the tidal dissipation is occurring at high temporal frequency. Furthermore, the viscosity in both the asthenosphere and the mantle of Io is held fixed in a statistically steady state to a distribution determined by that of the internal heating and the heat loss due to volcanic activity. On the very longest time scales it is therefore reasonable to assume that the tidal heating and the heat evacuation by volcanism are in balance ($\Phi_T - \Phi_V \approx 0$). This assumption is further supported by the fact that heat transported to the surface by volcanism is generally in excess of the heat transferred to the surface by conduction. The energy equation in the analyses to be discussed in what follows is solved by integration over cylindrical control volume elements and in time. In compact form we may then write:

$$\int_{\Delta V} \int_t^{t+\Delta t} \frac{\partial T}{\partial t} dt dv = \int_{\Delta V} \int_t^{t+\Delta t} G(T) dt dv, \tag{16}$$

where the function G includes all terms of Eq. (3) except for the partial time derivative of temperature. Integrating over volume and time, for each volume element we may write,

$$(T_P^1 - T_P^0)\Delta V = [\alpha G(T_P^1, T_N^1, T_S^1, T_B^1, T_T^1) + (1 - \alpha) G(T_P^0, T_N^0, T_S^0, T_B^0, T_T^0)]\Delta t \Delta V, \quad 0 \leqslant \alpha \leqslant 1. \tag{17}$$

The subscript P denotes the grid point at the center of the volume and N, S, B, and T stand for north, south, bottom, and top neighbor grid points. The superscripts 0 and 1 refer to the old value (known) and new value (unknown) of the temperature at time t and $t + \Delta t$ respectively. Here the weighting factor α (e.g. Patankar, 1980) enables us to have explicit solutions ($\alpha = 0$), fully implicit solutions ($\alpha = 1$) or semi-implicit solutions such as provided by the Crank–Nicolson scheme ($\alpha = 0.5$) or an arbitrary semi-implicit scheme. However in the present study we have solely employed the explicit scheme.

The energy equation at each grid point in the control volume formulation may then be rewritten in the form:

$$a_P T_P = a_N T_N + a_S T_S + a_B T_B + a_T T_T + b, \tag{18}$$

where a_P, a_N, a_S, a_B, and a_T are the coefficients of the temperatures at the center of volume, north, south, bottom and top neighbor grid points and b is the source term. The system of Eq. (18) is then solved using a power law scheme (Patankar, 1980) which suppresses unphysical variations in the temperature solution. In this formulation we have:

$$a_N = D_n A(|P_n|) + [[F_n, 0]], \tag{19a}$$

$$a_S = D_s A(|P_s|) + [[-F_s, 0]], \tag{19b}$$

$$a_B = D_b A(|P_b|) + [[F_b, 0]], \tag{19c}$$

$$a_T = D_t A(|P_t|) + [[-F_t, 0]], \tag{19d}$$

where we have used the notation $[[A, B]] \equiv \mathrm{Max}(A, B)$, and

$$P \equiv \frac{\rho V d}{\kappa} \quad \text{(Peclet number)}, \tag{20a}$$

$$F \equiv \rho V \quad \text{(Mass flux)}, \tag{20b}$$

$$D \equiv \frac{\kappa}{\delta x} \quad \text{(Diffusive conductance)}, \tag{20c}$$

$$A(|P|) = [[0, (1 - 0.1|P|)^5]] \quad \text{(Power–law)}. \tag{20d}$$

The lower case subscripts n, s, b, and t denote the quantity at the north, south, bottom and top volume boundaries respectively. Note that the $A(|P|) = 1$ limit represents the upwind advection scheme. The solution of the discretized equations is obtained using the Tri-Diagonal-Matrix Algorithm (TDMA) as described in Patankar (1980). The iterations are performed by sweeping the grid points in the radial and lateral directions alternatively. In order to take the effect of both boundary conditions into account (in each coordinate direction) on the discretized solutions, the grid points are swept back and forth in each iteration.

3. Design of the numerical experiments and model results

We have simulated the convection in the interior of Io in a cylindrical shell as noted above. Our focus here will be on simulations of the convection process in which an isothermal boundary condition is specified at the outer boundary. The corresponding condition at the inner boundary may be one of either constant temperature or zero heat flow.

Our model configuration is shown in Fig. 1. The geometry has been limited to encompass an azimuthal angle of $\pi/4$ in order to lower the computation time for the results to be presented herein. The numerical formulation includes depth dependent viscosity as illustrated in Fig. 2. The radial viscosity profiles in our numerical models are chosen so as to ensure the same thickness of asthenosphere in all three models with the prescribed smooth transition from low viscosity in the asthenosphere to the high viscosity in the lithosphere/crust. The viscosity in our model asthenosphere and mantle extend to 10^{12} Pa s and 10^{16} Pa s respectively. The particular form of the transition in viscosity from the asthenosphere to the mantle is chosen so as to ensure numerical stability. Since the

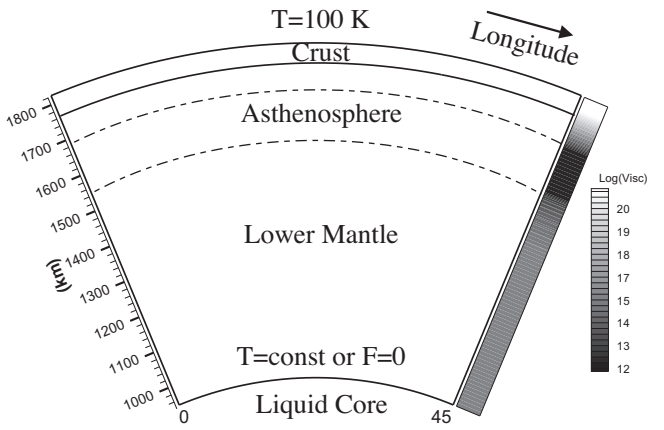

Fig. 1. Model setup – the dashed curves bracket the lowest viscosity region of the asthenosphere (10^{12} Pa s). The crust viscosities are 10^{21} Pa s, 10^{22} Pa s, and 10^{24} Pa s in our three models but the legend indicates the model with the crust viscosity of 10^{21} Pa s. The viscosity in the lower mantle is 10^{16} Pa s.

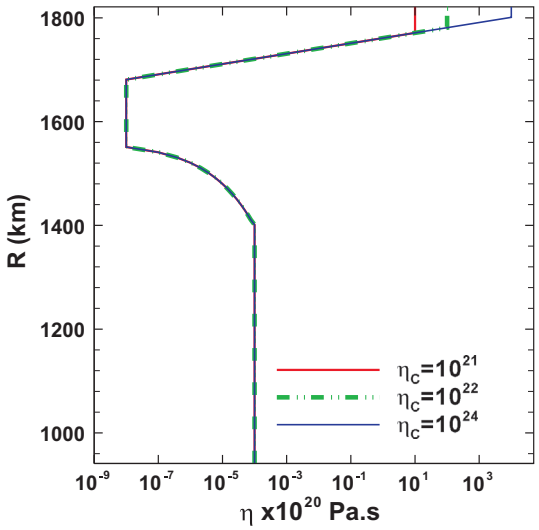

Fig. 2. Radial viscosity profiles used in our numerical models discussed in the text.

asthenospheric viscosity of Io is extremely low, there is a large contrast in the flow velocities between regions in the asthenosphere and those of the lithosphere/crust and upper mantle. This poses a challenging computational problem of time stepping which requires months of wall clock time for model runs of a few million years on a single processor even at lower grid resolutions. The numerical calculation at higher grid resolution required for this challenging problem is not computationally affordable at this time and the lower resolution grid calculations suffer somewhat from the influence of numerical diffusion. However, the horizontal scale of the cellular flow in the asthenosphere and therefore the horizontal scale of the surface features that this flow supports are determined by the thickness of this internal low viscosity region. The features of this length scale (~130 km) are adequately represented at first order by the grid resolutions we have employed in the framework of control volume formulation.

The calculation is initially performed on a 201 × 201 cylindrical grid with a radial resolution of ~4.4 km and lateral angular domain of width $\pi/4$ (Fig. 1). This resolution has been chosen to reduce the numerical calculation time and make the numerical calculations affordable with the present computational resources. However, the models were interpolated onto a higher resolution 401 × 401 grid once they reached to statistical equilibrium at lower spatial resolution. They were then further integrated for many millions of additional time steps, the additional evolution times extending a further 30,000 yr (for the models for which the tidal heating was not removed) or to 500,000 yr (for the models with 96% of the tidal dissipation removed). In none of the models was the variation in the surface heat flux or volumetric mean temperature found to be more than 1.2%. As it will be discussed in what follows the radial mass flux profiles demonstrate that the mass conservation constraint in our models is precisely satisfied.

The surface boundary condition is assumed to be rigid so as to resemble that which would be appropriate for a single plate planet and the side boundaries are free. The models include a crust/lithosphere of thickness 140 km, an asthenosphere of thickness 130 km, and a lower mantle of thickness of 610 km. The three models to be discussed in the first sequence upon which we will focus below differ in the thickness and the viscosity of the crust/lithospheric layer. The crustal thicknesses are assumed to be 20 km, 40 km, and 50 km in these three models in which the assumed viscosities are 10^{24} Pa s, 10^{22} Pa s, and 10^{21} Pa s respectively. While the crust viscosity in each model remains constant the viscosity of the lithosphere is assumed to linearly decrease with depth (Fig. 2). The temperature at the surface of Io is kept fixed to 100 K. The model parameters for the models discussed below are given in Table 1.

Starting from a sinusoidal temperature perturbation superimposed on a conduction solution, the model is run until the temporal averages of the mean temperature and boundary heat fluxes no longer show any significant long-term heating or cooling trends as well as no significant variation in the surface topography representing the statistical equilibrium of the model. Furthermore horizontal and vertical mass fluxes are monitored to ensure mass conservation is satisfied at each time step.

In the first sequence of models with the above specified crustal thicknesses, under the assumption that the tidal heating rate and the rate of heat transferred to the surface by volcanism are in balance, we also assume that they cancel each other locally ($\Phi_T(\bar{x}) - \Phi_V(\bar{x}) \approx 0$). A constant CMB temperature of 1500 K is assumed for this sequence of the models. The first model of this sequence has a crustal thickness of 50 km and viscosity of 10^{21} Pa s. The surface topography may be obtained by the balance between the normal stress at the surface and the gravitational force as:

$$h = -\frac{\tau_{rr}}{\rho g}. \tag{21}$$

In the earliest stages of evolution of this model, transient high and low topographies developed at the left and right boundaries. Subsequently but quite quickly after this long wavelength topography appeared, a short wavelength pattern developed that was superimposed upon this long wavelength pattern. The transient long wavelength topography disappeared rather quickly and the short wavelength features of the topography continued to develop.

The model was then run continuously for a long wall clock time up to its statistically steady state. Restarting from this statistical equilibrium model we ran two other models: one with a crust thickness of 40 km and the crustal viscosity of 10^{22} Pa s, and another with a crust of thickness 20 km and crustal viscosity of 10^{24} Pa s with the radial viscosity profiles displayed in Fig. 2. These models were integrated for 4 Myr of simulated time. No significant change in the amplitude of the surface topography in any of the models was observed following the first 2 Myr of model evolution. In all three models a layered state of small scale intra-lithospheric convection developed. A snapshot of the temperature field from the first model (having a 50 km thick crust), with the velocity arrows superimposed on the temperature field is shown in Fig. 3a. Compared to the depth of the asthenosphere the horizontal scale of the convection cells in the mantle is very large. As demonstrated in this figure, the asthenosphere of Io is dominated by vigorous short wavelength convection, but from time to time the small

Table 1
Physical properties of Io. The mean tidal heat dissipations are given for the models in which the heat is not removed. The values for the models in which the major part of the dissipation heat is removed are 4% of these values.

Radius	r_s	1821	km
Core radius	r_c	941	km
Surface temperature	T_s	100	K
Density	ρ	3270	kg/m^3
Gravitational acc.	g	1.8	m/s^2
Heat capacity	C_p	1200	J/kg/K
Thermal diffusivity	κ	1×10^{-6}	m^2/s
Thermal expansivity	α	3×10^{-5}	1/K
Ave tidal disp. (A)[a]	$\langle \Phi_T \rangle$	4.78×10^{-9}	W/kg
Ave tidal dip. (M)[b]	$\langle \Phi_T \rangle$	8.40×10^{-10}	W/kg

[a] Asthenosphere.
[b] Mantle.

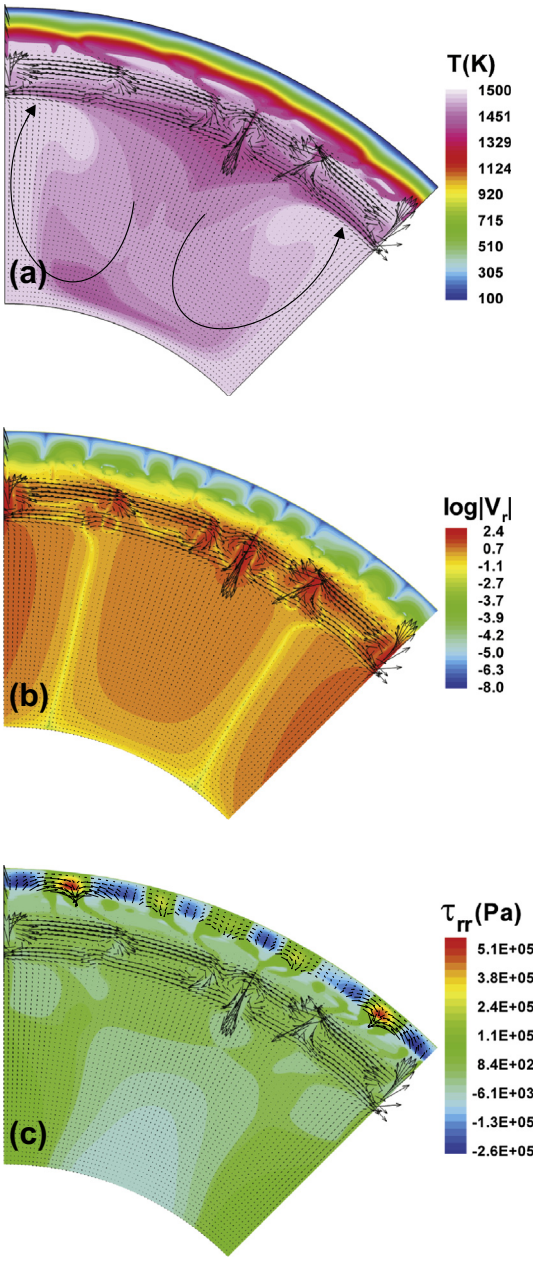

Fig. 3. (a) Snapshot of the temperature field (K) with superimposed velocity arrows at its statistically steady state, (b) the logarithm of the magnitude of the radial velocity field (m/yr) with the superimposed velocity arrows, and (c) normal stress field (Eq. (12)) in Pa for the snapshot shown in (a) with the superimposed velocities near the surface (different in scale).

convection cells merge to form a horizontally extended large aspect ratio convection cell within the asthenosphere. The magnitude of the velocity field with the superimposed velocity arrows is displayed in Fig. 3b. The velocity in the asthenosphere achieves a magnitude in excess of 250 m/yr while in the layered intra-lithospheric region it drops to a magnitude of order ~mm/yr or less. This can be verified by inspection of Fig. 3b which depicts the logarithm of the magnitude of the radial velocity field and demonstrates a large velocity contrast in the calculation domain due to the large viscosity variation throughout the lower mantle, asthenosphere and crust/lithosphere.

Because of the large viscosity contrast in the model domain the magnitude of the velocity near the surface is quite low (smaller by a factor of $\sim 10^8$ compared to that in the asthenosphere). The velocity arrows near the surface superimposed on the normal stress field (Eq. (12)) for this model are shown in Fig. 3c and clearly reveal the locations of the regions of uplift and subsidence. As can be inferred from the figure, despite high velocities in the planet's asthenosphere, there are no significant normal stresses acting on the lithosphere due to the fact that the viscosity at the base of lithosphere is relatively low. The only region characterized by relatively higher stress is the upper region of the lithosphere and crust where the viscosity is sufficiently high and where the short wavelength oscillations occur which translate into short wavelength surface topographic features. However the magnitude of the normal stress field near the surface is not sufficiently high to produce significant topography.

The influence of the increase in the viscosity of the crust on the magnitude of surface topography is shown in Fig. 4a. The surface topography in the model with a crust viscosity 10 times higher than our original model (10^{21} Pa s) has been diminished by about 20% while the other model with a crust viscosity 1000 times higher has a 50% reduction in the amplitude of the topography. The surface heat flux shown in this figure is that for the original model (50 km crust) displayed in Fig. 3 and is highly correlated to the developed short wavelength topography. Based on our model results the average heat flux at the surface of Io is about 45 mW/m^2, which is significantly below the observed Ionian surface heat flux. This is explained by the fact that the main cooling mechanism of Io is by volcanism (imposed by the condition $\Phi_T(\bar{x}) - \Phi_V(\bar{x}) \approx 0$) in the model) and the power radiated by the hot spots is essentially the total heat flow (Monnereau and Dubuffet, 2002).

In the second sequence of models a vertically nonuniform tidal dissipation in the interior of Io has been considered explicitly. Different regimes (Ross and Schubert, 1985; Ross et al., 1990) have been proposed for the tidal dissipation in the interior of Io. In our numerical models a heating mode in which a large amount of the heat is deposited in the asthenosphere of Io and which is mainly focused at the upper and the lower boundaries of asthenosphere, is assumed. We employ a depth dependent functional form (Tackley et al., 2001) with 2/3 and 1/3 dissipation rates in the asthenosphere and the mantle respectively as:

$$H(r) \sim \frac{0.4}{r^4}, \quad r < r_{asb}, \tag{22a}$$

$$H(r) \sim \frac{3}{1-\exp(-6)}\{\exp(-6z) + \exp[-6(1-z)]\}, \quad r_{asb} < r < r_{ast}, \tag{22b}$$

$$z = \frac{r_{ast} - r}{r_{ast} - r_{asb}}, \tag{22c}$$

where r_{asb} and r_{ast} are the radii at the base and top of the asthenosphere respectively. In this sequence of models the lateral variation in tidal heating is ignored. A tidal heating rate of 100 TW (Veeder et al., 1994) has been assumed and has been normalized to the prescribed cylindrical geometry as displayed in Fig. 1. The models in this sequence have a crustal thickness of 50 km and viscosity of 10^{21} Pa s and only differ from one another in terms of the heat removal mechanism. Due to the small size and the high rate of tidal heating in the interior of Io, the core and mantle of Io are assumed to be in thermal equilibrium. In this and the following sequence of models zero heat flux at the core–mantle boundary is assumed. The dominant fraction of the heat generated by the tidal dissipation is transferred to the surface by volcanism which is extracted from the base of lithosphere and transferred to the surface by volcanic vents and conduits.

Two end member models have been considered. In the first model the generated heat is not removed and the planet radiates

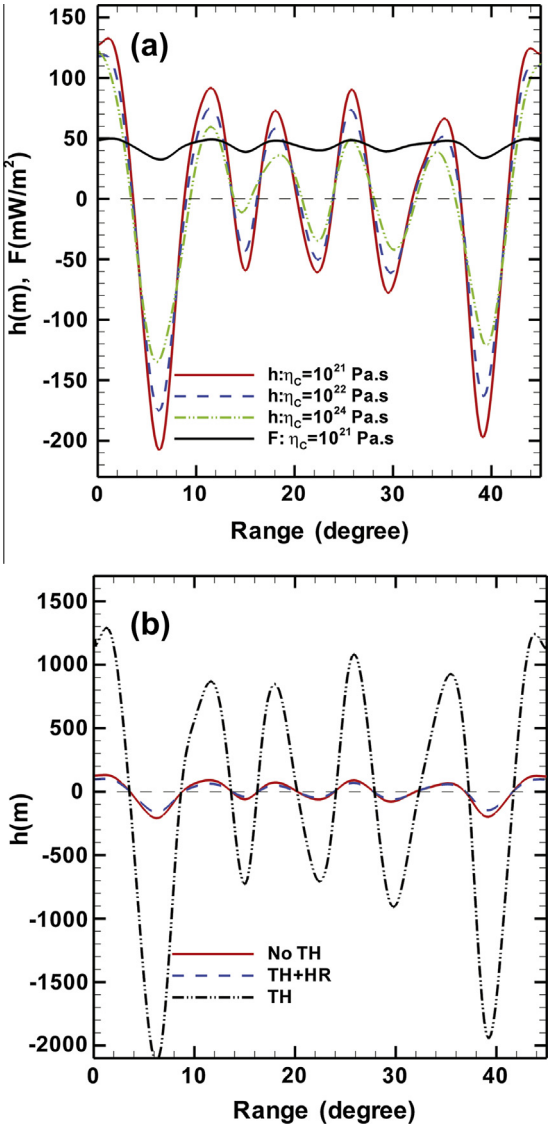

Fig. 4. (a) Surface topography for the first sequence of models with crust viscosities of 10^{21} Pa s, 10^{22} Pa s, and 10^{24} Pa s, and heat flux for the original model with 50 km crustal thickness ($\eta = 10^{21}$ Pa s), at their statistically steady state. The topography has an average 280 km wavelength and is highly correlated with the surface heat flux. (b) The surface topography of the first model from the first sequence of models (NO TH) is compared with the surface topography of the models from the second sequence of models with tidal heating. NO TH, TH + HR and TH refer to no tidal heating, tidal heating with 96% of the heat removed and tidal heating with no heat removal respectively.

the heat from the surface only by conduction. In the second model we assume a heat removal functional form which is proportional to the tidal heat generation rate. In the latter case the amount of heat removed from the mantle and asthenosphere is 96% of the heat generated by tidal heating. The remaining heat is therefore transferred to the upper levels by convection and radiates from the surface by conduction. This case resembles a model in which the heat is assumed to be transferred to the base of lithosphere by melt migration in the asthenosphere and then be transported to the surface by heat pipes (Moore, 2001, 2003). Our numerical models reveal that the small scale circulation persists in both of these models. Fig. 5a and c display snapshots of these two models. However, compared to the model with the crustal thickness of 50 km in the first sequence of models the topography has increased/diminished by a factor of ~11/1.4 in the first and second models of this sequence, respectively (Fig. 4b). The average and maximum velocity profiles of these models are compared with the main model (50 km crust) in the first sequence of models in Fig. 6. These model results demonstrate that either in the absence or presence of explicit tidal heating small scale convection cells develop in the asthenosphere of Io which is reflected in the surficial features. From Fig. 6 it could be conjectured that compared to the main model of the first sequence the maximum velocity has increased/diminished by a factor of ~8/1.4 in the first and second models of this sequence respectively. From Fig. 6 it can also be verified that the average velocities in the case of the model with 96% tidal heating removed and the case with full tidal heating reach approximately 50 m/yr and 250 m/yr respectively. These models are different in Rayleigh number by a factor of about 25 due to the difference in the rate of tidal heating. The change in the velocities is consistent with the theoretical prediction $V \sim Ra_H^{0.5}$ (Turcotte and Schubert, 1982) which demonstrates the sensitivity of our model results to the Rayleigh number in spite of the relatively low grid resolution which we are restricted to employ. Furthermore the magnitudes of the velocities are also consistent with previous numerical predictions based upon the application of a scaling argument (Tackley, 2001; Tackley et al., 2001). As a resolution test the model in which 96% of the tidal heating is removed is tested on 101×101, 201×201, 401×401 and 601×601 grid resolutions. The mass nonconservation at these grid resolutions are about 8%, 3%, 0.5% and 0.2% respectively. Except for the first grid resolution the difference in mean temperatures in the last three grid resolutions are less than one percent.

In our third sequence of models we also consider lateral variations in tidal dissipation in the asthenosphere in addition to the radial variations introduced in the previous sequence. The two models of this sequence are similar to the models in the second sequence except for the additional lateral variations in tidal heating. A lateral variation in heat dissipation of the form:

$$H(\theta) = 1 + Cos\left(\frac{\pi\theta}{\theta_{Max}}\right), \tag{23}$$

is assumed and which has its maximum at the left boundary. Snapshots of the temperature fields of these models are displayed in Fig. 5b and d. Starting from the previous models of the second sequence (with radial variations in heat dissipation but no lateral variations) in their statistically steady state and imposing lateral variations in tidal dissipation a transient increase in core–mantle topography by a maximum of approximately 12% develops. However, following a very brief period of temporal evolution the difference in core–mantle boundary topography between these model variants (with and without lateral variations in tidal heating) was found to be insignificant. Compared to the previous models we also observed no significant change in the surface topography. This is understandable by virtue of the fact that the impact of the large scale lateral variations in tidal dissipation in the asthenosphere of Io on mean heat flux decreases as the Rayleigh number increases. As illustrated in Fig. 3 of Tackley (2001) whereas at $Ra = 10^7$ the mean heat flux at the left boundary is more than three times that at the right boundary, this difference is reduced to 20% at $Ra = 10^{10}$ and is expected to entirely negligible at $Ra = 10^{12}$ due to the increased efficiency of mixing in the asthenosphere at higher Rayleigh numbers. Similarly in Fig. 7 of Tackley et al. (2001) while there is a significant contrast between the extrema in the surface, base-of-lithosphere and CMB heat fluxes at $Ra = 10^4$, the contrast is significantly diminished at $Ra = 10^7$ and is expected to be insignificant at $Ra = 10^{12}$.

In order to examine the impact of the asthenosphere viscosity on mixing in the asthenosphere and consequently on the long wavelength characteristics of the surface topography which

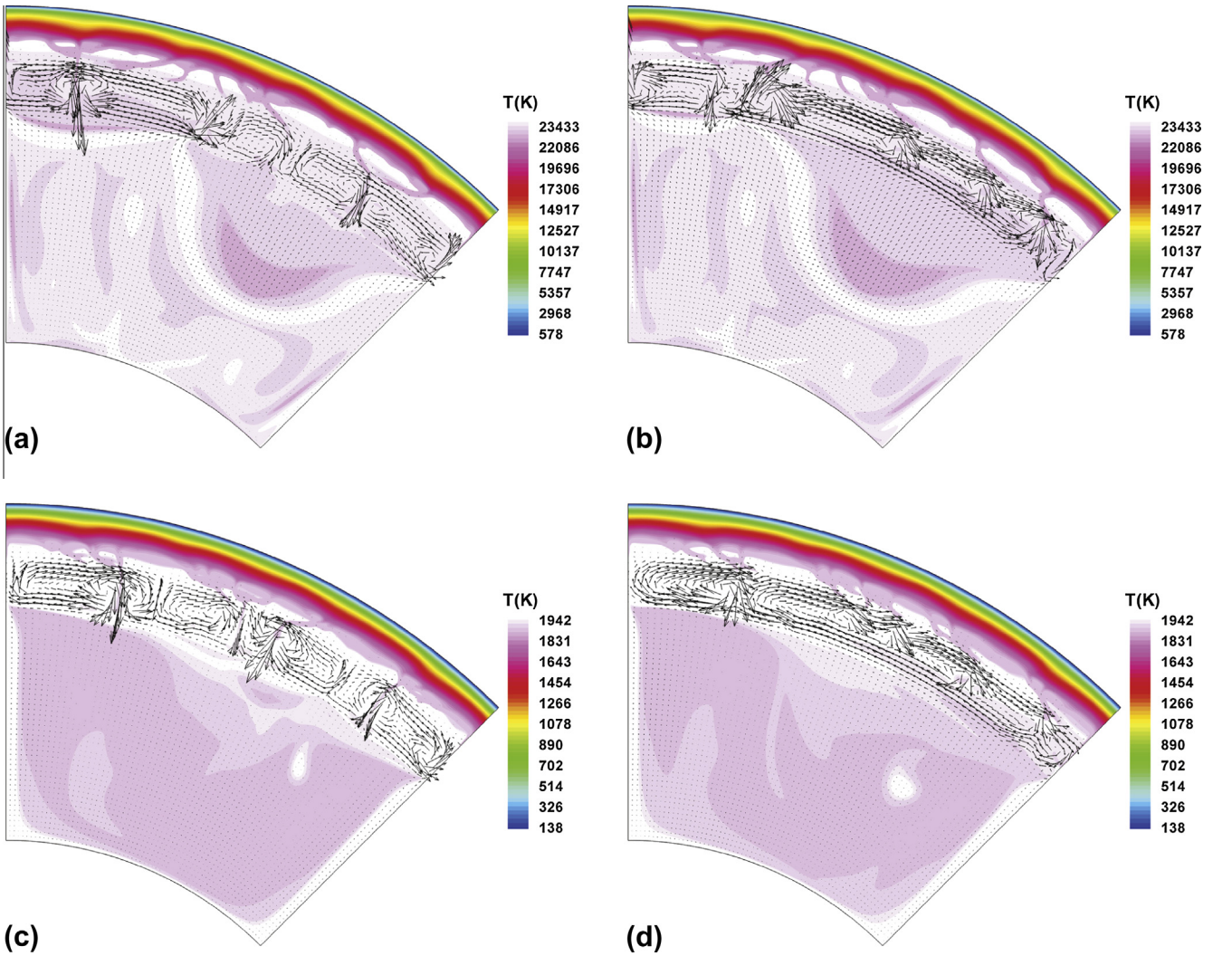

Fig. 5. Snapshots of the temperature fields with superimposed velocity arrows at their statistically steady state for the model (a) with 10^{14} TW radial tidal heating in mantle and asthenosphere, (b) similar to (a) but the lateral variations in tidal dissipation is also considered, (c) similar to (a) but the tidal dissipation is reduced by 96%, and (d) similar to (b) but the tidal dissipation is reduced by 96%.

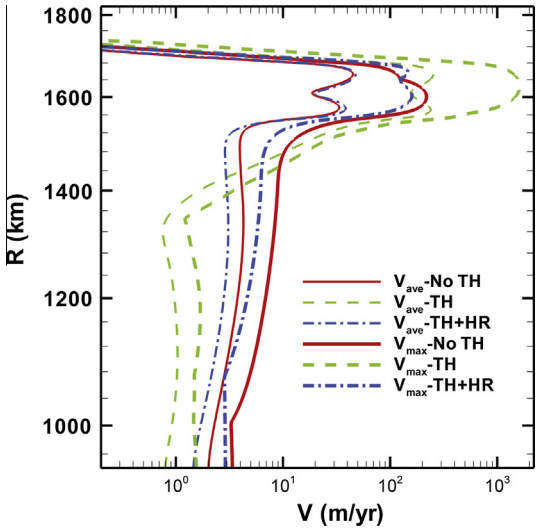

Fig. 6. The laterally averaged and maximum velocity profiles for the main model from the first sequence and the models from the second sequence of models. NO TH, TH + HR and TH refer to no tidal heating, tidal heating with 96% of the heat removed and tidal heating with no heat removal respectively.

originates from the lateral variations in tidal heating dissipation, we set three more models with higher asthenosphere viscosity. We increased the viscosity in the asthenosphere in the reference model with tidal heating removed by 96% (third sequence) by a factor of 10, 100 and 1000 in the three models of this sequence. Compared to the reference model we did not observe a significant change in the surface topography in the model with higher viscosity in the asthenosphere by a factor of 10 after 1.5 Myr of evolution. In the second model with higher asthenosphere viscosity by a factor of 100 we observed 4% asymmetry (defined as the variation in surface topography between the left and right boundaries with respect to the peak to peak magnitude of the topography) in surface topography between the right and left boundary after 7 Myr evolution time. In the last model with a more viscous asthenosphere (1000 times higher compared to the reference model) the asymmetry in surface topography between the right and left boundary was found to be about 47% after 23 Myr of evolution. These topographies are compared with the topography of the reference model in Fig. 7.

Finally we show that not only is the energy conservation constraint well satisfied by our models (which requires a balance between the tidal dissipation heating and the surface heat flux) but also the mass conservation constraint. To demonstrate the latter we have compared the cumulative radial mass flux profiles

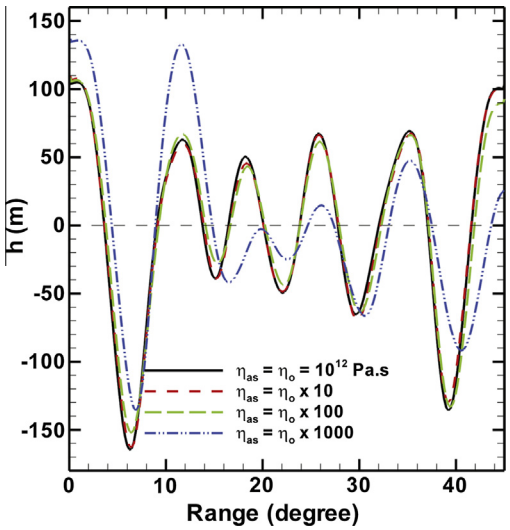

Fig. 7. Surface topographies in the models with higher viscosity asthenosphere are compared with the surface topography of the reference model (third sequence). In all models 96% of the tidal heating is removed and the tidal dissipation varies laterally.

(laterally averaged upward and downward fluxes through each control volume) and the absolute radial mass flux profiles in Fig. 8 for the models discussed in the third sequence. The figure reveals that the maximum mass-nonconservation which occurs at the boundaries of the asthenosphere, in the worst case is less than 1% which is remarkable for the extremely variable viscosity profile we employ together with the spatial resolution.

4. Discussion and conclusions

The enhanced tidal heating associated with Io's orbital eccentricity makes Io one of the most volcanically active planets in our Solar System with hundreds of volcanic centers of activity. The high rate of resurfacing of Io by lava flows and sulfurous plume deposits obscures the tectonic features and the mechanism responsible for the formation of high mountains on Io is not yet well understood. Nevertheless, three more distinct type of topography may be identified: elevations of the north and south poles which are moderately high and low respectively; topography in the equatorial region which consists of four alternating long wavelength high and low regions; and distributed short wavelength topography that is well correlated with the observed surface heat flux.

Based on the observations of the near-infrared mapping spectrometer (NIMS), results from the Solid State Imaging System (SSI) and from ground based observations; Lopes-Gautier et al. (1999) identified 61 active volcanic centers. Their detection methodology for 41 hot spots was based on NIMS and/or SSI, while the remainder of the hot spots was detected mainly on the basis surface changes. Their analysis shows that the distribution of the persistently active hot spot centers (with the activity period ranging from months to years) does not reveal any clear correlation with latitude or longitude, Voyager-derived planetary topography (Fig. 9a, reconstructed from Ross et al., 1990), or heat flow patterns from the asthenosphere and deep mantle tidal dissipation model predictions. The persistent hot spot and active plume distribution (concentrated toward lower latitudes), however, is somewhat consistent with the asthenosphere rather than the deep mantle dissipation model but the agreement is poor. Fig. 9b and c presents a reproduction, of the panels of Fig. 5 of Lopes-Gautier et al. (1999) in which the active volcanic centers are superimposed over the heat flow patterns predicted by Ross et al. (1990). In Fig. 9b the identified hot spots (plus signs) are superimposed on the heat flow patterns derived from deep mantle tidal dissipation models, whereas in Fig. 9c the heat flow pattern is based on the asthenosphere tidal dissipation model of Ross et al. (1990). As can be inferred from the second and third panels of this figure, the observed hot spots are not well correlated with the heat flow map.

A more recent spectral analysis based on spherical harmonics (Kirchoff et al., 2011) reveals a strong degree-2 component in the distribution of volcanic centers consistent with asthenospheric or predominantly asthenospheric tidal heating in which the maximum heating is generated at two regions longitudinally separated by 180° (Fig. 9c) near the equatorial region. This degree 2 spatial distribution in volcanic centers is shown by red zones in Fig. 10b (Kirchoff et al., 2011). The analysis reveals that at higher degrees the spectrum is white, indicating the randomness of the distribution. Their study also shows that, based on the volcanic and high topography features identified by Schenk et al. (2001), at low degrees the volcanic and mountainous distributions are anti-correlated (Fig. 10). Fig. 11 is a reproduction of Fig. 3 of Rathbun et al. (2004) and displays the high resolution composite temperature map for Io, derived from different observations (the night-time effective temperature photopolarimeter–radiometer (PPR) open filter, superimposed on a solid state image (SSI) map). Due to Galileo viewing limitations (Jupiter-facing hemisphere at night), only the longitude range 150–360° is shown. The average wavelength of the hot spots displayed in this map is consistent with the topography and heat flow spatial scale predicted by our layered model results shown in Figs. 3–5, and 7 (∼9°). Small scale convection in the asthenosphere may therefore account for the short wavelength surficial features of Io.

Previous numerical studies that rely on isostatic adjustment and the assumption of isostatic compensation of the long-wavelength topography and ignore the impact of convection on surface topography (Ross et al., 1990) have suggested the applicability of two different models: the thermal swell model and the differentiated lithosphere model. Their calculations are based on heat flow calculations with assumed rates of tidal dissipation in a viscous asthenosphere and deep mantle (which are assumed to account for 2/3 and 1/3 of the heating respectively). In the thermal swell model, the composition of the lithosphere and the asthenosphere is assumed to be the same and the lithosphere is thermally higher in density by 1.6% (Gaskell et al., 1988). In the differentiated lithosphere model the lithosphere is assumed to be lower in density by 7%. The thermal swell model results in a positive correlation between the heat flow and topographic elevation, while in the differentiated lithosphere model the heat flow and topography are anti-correlated. These two model topographies can show positive correlation with the observed long wavelength topography of Io (Fig. 9a) if they are rotated longitudinally by 25° (greater longitudes) and −25° (smaller longitudes) in the case of the differentiated lithosphere model topography (Fig. 3b of Ross et al., 1990) and the thermal swell lithosphere model topography (Fig. 4b of Ross et al., 1990), respectively. However, the preferred model of these authors is the differentiated lithosphere model suggesting a zonal rotation toward the smaller longitudes. Such a zonal rotation could conceivably occur due to an exchange of spin angular momentum between the lithosphere and asthenosphere. Despite the partial successes of these models in predicting the general features of the long wavelength topography of Io neither has been able to explain the short wavelength characteristics of the surface heat flow.

Other numerical convection models with tidal dissipative heating in the asthenosphere and mantle (Tackley et al., 2001) provide similar heat flow patterns of long wavelength. Owing to the high rate of tidal heating in the interior of Io, which requires modeling at very high Rayleigh numbers, and due to the fact that there is very large viscosity variation in the interior of Io, numerical

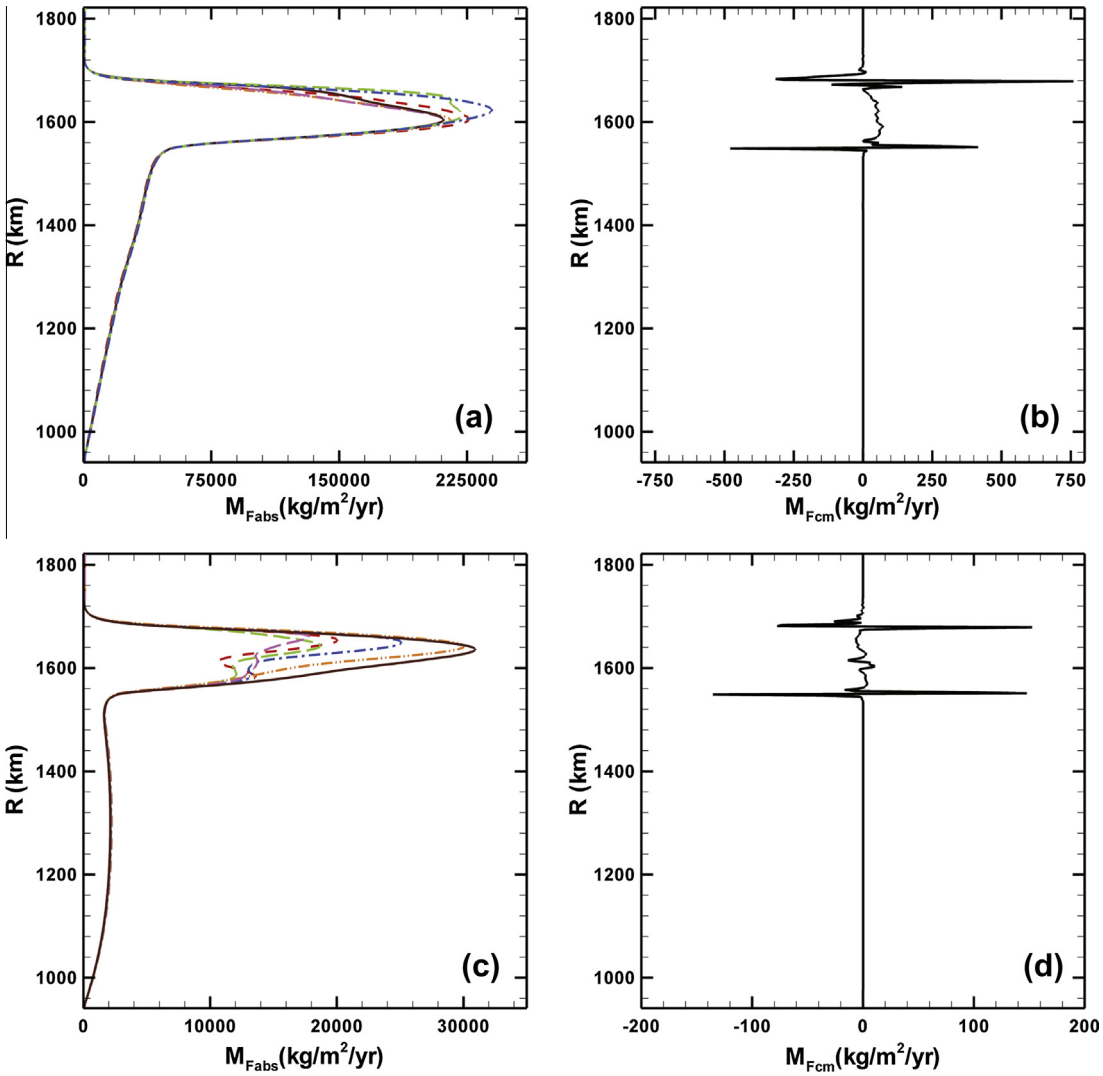

Fig. 8. (a) Absolute radial mass flux profiles at few evolution times for the model with no heat removed, (b) cumulative radial mass profile at a single snapshot for the model with no heat removed, (c) similar to (a) but for the model with 96% heat removed, and (d) similar to (b) but for the model with 96% heat removed.

modeling of the dynamics is a challenging problem. The previous work on Io convection relies upon application of a scaling scheme, the goal of which is to reduce the Rayleigh number. In this study we have employed a control volume formulation of the convection problem which enables us to treat large viscosity contrasts at high Rayleigh number explicitly. Using it we have investigated the style of convection in the interior of Io and its impact on surficial features.

Our modeling results demonstrate that the short wavelength that is characteristic of Ionian surface heat flux is expected to be well correlated with the layered intra-lithospheric small-scale convection (LILSSC) in Io. Four sequences of models were designed to understand the style of convection in the interior of Io with large variations of viscosity and a very low viscosity asthenosphere. In the first sequence of models the internal heating was ignored and the model results revealed that small-scale convection developed in the asthenosphere of the planet which directly impacts the surface heat flow distribution. Small scale convection in the asthenosphere of Io persisted in the second sequence of models where a tidal heating rate with the proportionality of 2/3 and 1/3 was included in the asthenosphere and lower mantle respectively. Compared to the model in which the tidal heating is present but is not removed from the interior of Io, the maximum velocity in the asthenosphere and surface topography for the model in which the majority of the tidal heating (96%) was removed from the interior of planet are low by a factor of 10 and 15, respectively (Figs. 6 and 4b). Based on a scaling method extrapolating from low Rayleigh numbers to high Rayleigh numbers, the Cartesian models of Tackley et al. (2001) predict mean flow velocities of 50–5600 m/yr.

Our model results suggest that the short wavelength topography of Io that is correlated to the observed heat flow cannot exceed a few hundreds of meters in height which is within the error estimates of the observations. The expected short wavelength portion of the surface topography may be explained by small-scale convection cells in the satellite's asthenosphere which are triggered by the thermal instabilities that develop at its upper boundary. These instabilities are therefore transferred by small scale convection to the base of the asthenosphere, and are in turn responsible for triggering long wavelength convection in the Ionian mantle (due to the viscosity contrast between the Ionian asthenosphere and mantle). The large scale features of the Ionian topography, however, may be accounted for either by a model involving isostatic compensation or by the large scale convection originating from the asthenosphere or mantle which modulates the small scale features generated by the small scale convection cells. In the preferred model of Tackley et al. (2001) designed on the basis of that of Ross et al.

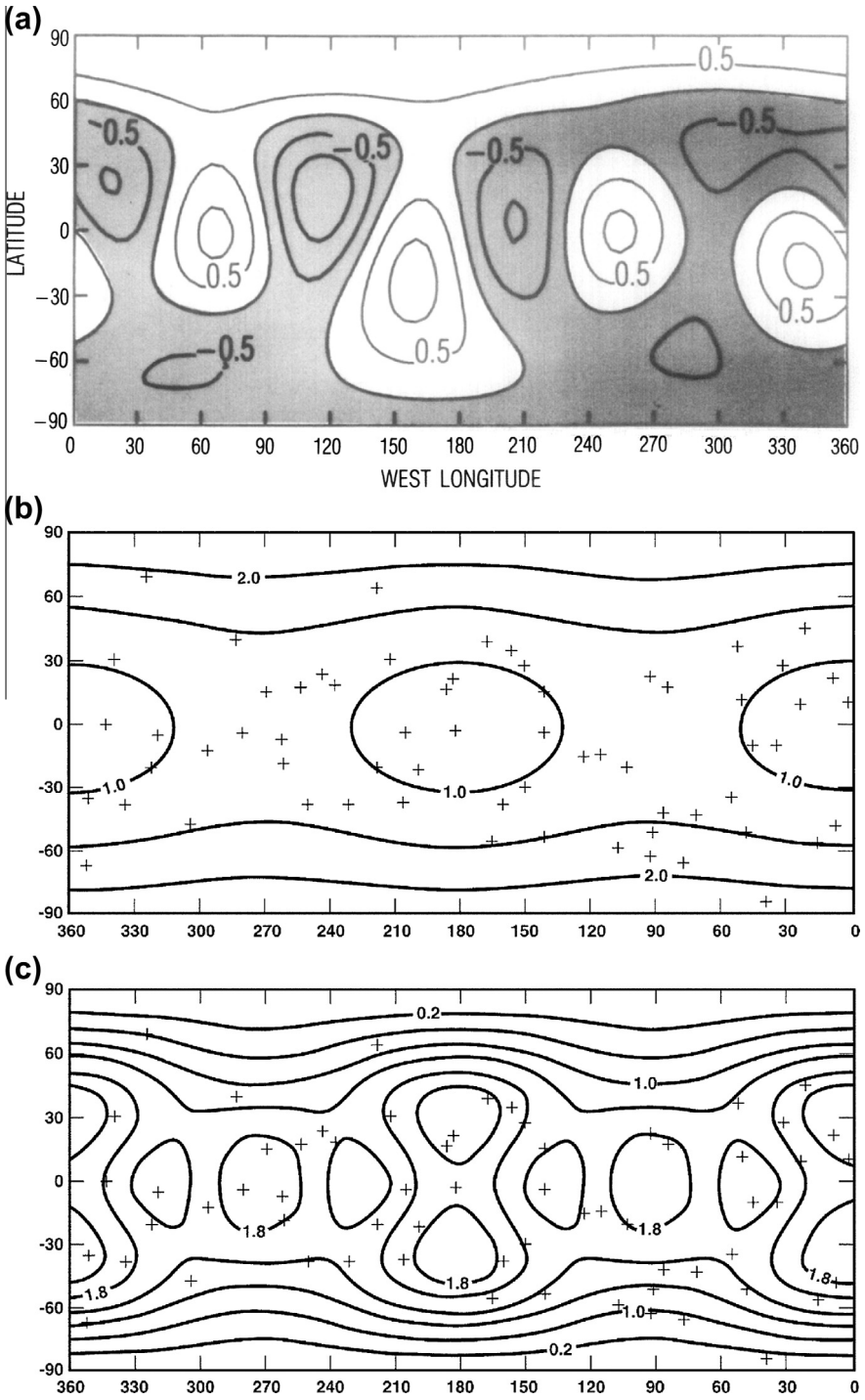

Fig. 9. (a) Contour map of the elevation (in km) of Io's surface with respect to the reference triaxial ellipsoid based on a spherical harmonic representation up to degree 4 (reconstructed from Ross et al. (1990)), (b) deep-mantle tidal dissipation model, and (c) asthenosphere tidal dissipation model (heat flow contours in watts per meter squared). Active volcanic centers (reconstructed form Lopes-Gautier et al. (1999)) are superimposed over the heat flow patterns predicted by Ross et al. (1990).

(1990), with 1/3 mantle and 2/3 asthenosphere heating distribution, the wavelength describing the characteristic length between the heat flux minima and maxima is larger than the characteristic wavelength describing the spacing between the hot spot peaks at the surface of Io (Rathbun et al., 2004); their model results nevertheless appear to produce a reasonable fit to the general features of the long wavelength topography.

Our model results reveal that the long wavelength of the surface topography of Io may be correlated to the lateral variations of the tidal dissipation in the asthenosphere (Tackley, 2001; Tackley et al., 2001). This depends on the viscosity in the asthenosphere region being at least two orders of magnitude higher than the previous estimations. Lower values of the viscosity in the asthenosphere of Io enhance mixing in the asthenosphere which diminishes the impact of lateral variation in tidal heating on the surface long wavelength topography. An alternative possibility is that the long wavelength surface topography originates from the mantle, however, since a very low viscous asthenosphere can buffer mantle from the lithosphere a higher viscosity asthenosphere is more plausible.

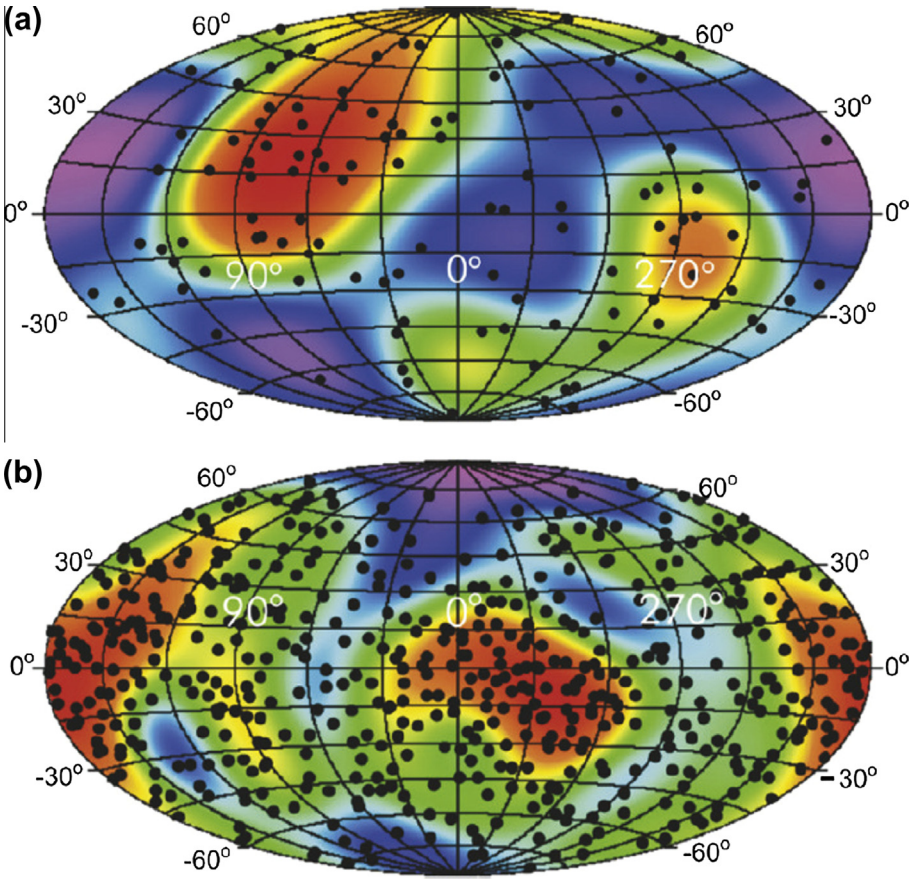

Fig. 10. (a) Hammer equal area projection of the spherical harmonic representation of the equally weighted mountain distributions truncated at $l = 4$. (b) Hammer equal area projection of the spherical harmonic representation of the total volcanic center distribution truncated at $l = 6$. Red colors indicate more dense concentrations and blue colors indicate relatively less dense concentrations. Black dots represent the actual positions of the mountains (a) or volcanic centers and paterae (b). Reproduced from Kirchoff et al. (2011).

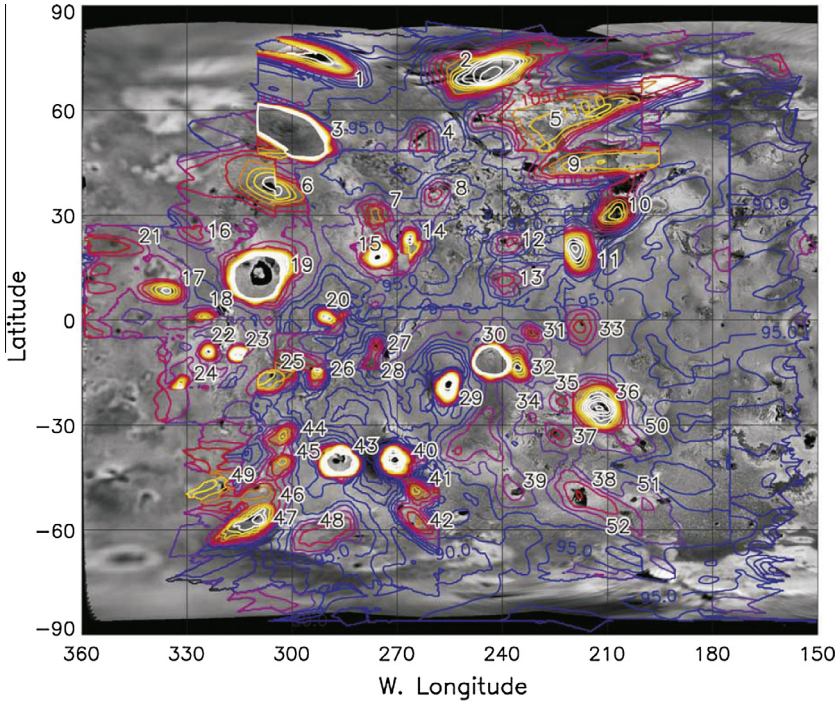

Fig. 11. Map of night-time effective temperature in PPR open filter, superimposed on an SSI map of Io. Hot spots observed near Io's limb are elongated perpendicular to the limb when projected onto the map. Contour interval is 2.5 K, and contours above 130 K are omitted to avoid hiding the sources of the brightest hot spots. The figure is taken from Rathbun et al. (2004). For the labels of hot spots and other details refer to this reference.

Further analyses will be necessary to more fully understand the nature of the coupling between the small scale and large scale dynamics and the relation to surface features. Our control volume models also suggest that the Ionian high mountains cannot be produced by the mantle or intra-lithospheric upwelling plumes alone. Other mechanisms, most likely including distinct tectonic events must be responsible for the highest surficial features on Io. Among a number of tectonic mechanisms yet to be studied, the scenario of a faulted crust which is under compression due to the subsidence caused by the uniform global volcanic resurfacing appears to be the more plausible (Turtle et al., 2001).

References

Anderson, J.D., Sjogren, W.L., Schubert, G., 1996. Galileo gravity results and the internal structure of Io. Science 272, 709–710.

Anderson, J.D., Jacobson, R.A., Lau, E.L., 2001. Io's gravity field and interior structure. J. Geophys. Res. 106, 32963–32970.

Blaney, D.L., Johnson, T.V., Matson, D.L., Veeder, G.L., 1995. Volcanic eruptions on Io: Heat flow, resurfacing, and lava composition. Icarus 113, 220–225.

Carr, M.H., 1986. Silicate volcanism on Io. J. Geophys. Res. 91, 3521–3532.

Cassen, P.M., Peale, S.J., Reynolds, R.T., 1982. Structure and thermal evolution of the Galilean satellites. In: Morrison, D. (Ed.), Satellites of Jupiter. The University of Arizona Press, Tucson, pp. 93–128.

Davies, A.G. et al., 2001. Thermal signature, eruption style, and eruption evolution at Pele and Pillan on Io. J. Geophys. Res. 106 (E12), 33079–33103.

Fischer, H.J., Spohn, T., 1990. Thermal–orbital histories of viscoelastic models of Io (J1). Icarus 83, 39–65.

Gaskell, R.W., Synnott, S.P., McEwen, A.S., Schaber, G., 1988. Large scale topography of Iv: Implications for internal structure and heat transfer. Geophys. Res. Lett. 15, 581–584.

Geissler, P.E., McEwen, A.S., Keszthelyi, L., Lopes-Gautier, R., Granahan, J., Simonelli, D.P., 1999. Global color variations on Io. Icarus 140, 265–282.

Harder, H., Hansen, U., 2005. A finite-volume solution method for thermal convection and dynamo problems in spherical shells. Geophys. J. Int. 161, 522–537.

Jaeger, W.L., Turtle, E.P., Keszthelyi, L.P., Radebaugh, 1.J., McEwen, A.S., 2003. Orogenic tectonism on Io. J. Geophys. Res. 108 (E8), 5093. http://dx.doi.org/10.1029/2002JE001946.

Johnson, T.V., Cook II, A.F., Sagan, C., Soderblom, L.A., 1979. Volcanic resurfacing rates and implications for volatiles on Io. Nature 280, 746–750.

Keszthelyi, L., McEwen, A.S., 1997. Magmatic differentiation of Io. Icarus 130, 437–448.

Keszthelyi, L., McEwen, A.S., Taylor, G.J., 1999. Note: Revisiting the hypothesis of a mushy global magma ocean in Io. Icarus 141, 415–419.

Keszthelyi, L., Jaeger, W.L., McEwen, A.S., Turtle, E.P., 2003. Io's interior: A synthesis view at the end of the Galileo era. Lunar Planet. Sci. XXXIV.

Keszthelyi, L., Jaeger, W.L., Turtle, E.P., Milazzo, M., Radebaugh, J., 2004. A post-Galileo view of Io's interior. Icarus 169, 271–286.

Kirchoff, Michelle R., McKinnon, William B., Schenk, Paul M., 2011. Global distribution of volcanic centers and mountains on Io: Control by asthenospheric heating and implications for mountain formation. Earth Planet. Sci. Lett. 301, 22–30.

Kivelson, M.G., Khurana, K.K., Volwerk, M., 2002. The permanent and inductive magnetic moments of Ganymede. Icarus 157, 507–522.

Kuskov, Oleg L., Kronrod, Victor A., 2000. Resemblance and difference between the constitution of the Moon and Io. Planet. Space Sci. 48, 717–726.

Lieske, J.K., 1980. Improved ephemerides of the Galilean satellites. Astron. Astrophys. 82, 340–348.

Lopes-Gautier, R., McEwen, A.S., Smythe, W.B., Geissler, P.E., Kamp, L., Davies, A.G., Spencer, J.R., Keszthelyi, L., Carlson, R., Leader, F.E., Mehlman, R., Soderblom, L., 1999. Active volcanism on Io: Global distribution and variations in activity. Icarus 140, 243–264.

Lunine, J., Stevenson, D., 1985. Physics and chemistry of sulfur lakes on Io. Icarus 64, 345–367.

McEwen, A.S., Keszthelyi, L., Geissler, P., Simonelli, D.P., Carr, M.H., Johnson, T.V., Klaasen, K.P., Breneman, H.H., Jones, T.J., Kaufman, J.M., Magee, K.P., Senske, D.A., Belton, M.J.S., Schubert, G., 1998a. Active volcanism on Io as seen by Galileo SSI. Icarus 135, 181–219.

McEwen, A.S. et al., 1998b. High-temperature silicate volcanism on Jupiter's moon Io. Science 281, 87–90.

Monnereau, M., Dubuffet, F., 2002. Is Io's mantle really molten? Icarus 158, 450–459.

Moore, W.B., 2001. Note: The thermal state of Io. Icarus 154, 548–550.

Moore, W.B., 2003. Note: Tidal heating and convection in Io. J. Geophys. Res. 108 (E8), 5096, http://dx.doi.org/10.1029/2002JE001943.

Nash, D.B., Carr, M., Gradie, J., Hunten, D., Yoder, C., 1986. Io. In: Burns, J., Matthews, M. (Eds.), Satellites. The University of Arizona Press, Tucson.

Ogawa, M., Schubert, G., Zebib, A., 1991. Numerical simulations of 3-dimensional thermal convection in a fluid with strongly temperature-dependent viscosity. J. Fluid Mech. 233, 299–328.

O'Reilly, T.C., Davies, G.F., 1981. Magma transport of heat on Io: A mechanism allowing a thick lithosphere. Geophys. Res. Lett. 8, 313–316.

Patankar, S.V., 1980. Numerical Heat Transfer and Fluid Flow. McGraw-Hill, New York.

Patankar, S.V., Spalding, D.B., 1972. A calculation procedure for heat, ass and momentum transfer in three-dimensional parabolic flows. Int. J. Heat Mass Trans. 15, 1787–1806 (Pergamon Press).

Peale, S.J., Cassen, P., Reynolds, R.T., 1979. Melting of Io by tidal dissipation. Science 203, 892–894.

Phillips, C.B., 2000. Voyager and Galileo Views of Volcanic Resurfacing on Io and the Search for Geologic Activity on Europa. Ph.D. Thesis, Univ. of Ariz., Tucson.

Ratcliff, J.T., Schubert, G., Zebib, A., 1996. Effects of temperature-dependent viscosity on thermal convection in a spherical shell. Physica D 97 (1–3), 242–252.

Rathbun, J.A., Spencer, J.R., Tamppari, L.K., Martin, T.Z., Barnard, L., Travis, L.D., 2004. Mapping of Io's thermal radiation by the Galileo photopolarimeter–radiometer (PPR) instrument. Icarus 169, 127–139.

Ross, M.N., Schubert, G., 1985. Tidally forced viscous heating in a partially molten Io. Icarus 64, 391–400.

Ross, M.N., Schubert, G., 1986. Tidal dissipation in a viscoelastic planet. J. Geophys. Res. 91, D447–D452.

Ross, M.N., Schubert, G., Spohn, T., Gaskell, R.W., 1990. Internal structure of Io and the global distribution of its topography. Icarus 85, 309–325.

Schenk, P.M., Bulmer, M.H., 1998. Origin of mountains on Io by thrust faulting and large-scale mass movements. Science 279, 1514–1517.

Schenk, P.M., Hargitai, H., Wilson, R., McEwen, A., Thomas, P., 2001. The mountains of Io: Global and geologic perspectives from Voyager and Galileo. J. Geophys. Res. 106, 33201–33222.

Schubert, G., Stevenson, D., Ellsworth, K., 1981. Internal structure of the Galilean satellites. Icarus 47, 46–59.

Schubert, G., Spohn, T., Reynolds, R.T., 1986. Thermal histories, compositions, and internal structures of the moons of the Solar System. In: Burns, J., Matthews, M. (Eds.), Satellites. The University of Arizona Press, Tucson.

Segatz, M., Spohn, T., 1988. Io: Tidal dissipation and convective heat transfer. EOS 69, 1297.

Segatz, M., Spohn, T., Ross, M., Schubert, G., 1988. Tidal dissipation, surface heat flow and figure of viscoelastic models of Io. Icarus 75, 187–206.

Shahnas, M.H., Peltier, W.R., 2010. Layered convection and the impacts of the perovskite–postperovskite phase transition on mantle dynamics under isochemical conditions. J. Geophys. Res. 115, B11408, http://dx.doi.org/10.1029/2009JB007199.

Sinton, W.M., 1982. Io: A volcanic flow model for the hot spot emission spectrum and a thermostatic mechanism. Icarus 51, 563–573.

Smith, B.A. et al., 1979. The Jupiter system through the eyes of Voyager 1. Science 204, 951–972.

Spencer, J.R., Schneider, N.M., 1996. Io on the eve of the Galileo mission. Annu. Rev. Earth Planet. Sci. 24, 125–190.

Spohn, T., 1997. Tides of Io. In: Wilhelm, H., Zürn, W., Wenzel, H.-G. (Eds.), Tidal Phenomena. Springer-Verlag, Berlin, pp. 345–377.

Stemmer, K., Harder, H., Hansen, U., 2006. A new method to simulate convection with strongly temperature-dependent and pressure-dependent viscosity in a spherical shell: Applications to the Earth's mantle. Phys. Earth Planet. Interiors 157, 223–249.

Tackley, P.J., 1994. Three-dimensional Models of Mantle Convection: Influence of Phase Transitions and Temperature-Dependent Viscosity. Ph.D. Thesis, California Institute of Technology, Pasadena.

Tackley, P.J., 1998. Three-dimensional simulations of mantle convection with a thermochemical CMB boundary layer: D"? In: Gurnis et al. (Eds.), The Core–Mantle Boundary Region. American Geophysical Union, pp. 231–253.

Tackley, P.J., 2001. Convection in Io's asthenosphere: Redistribution of non-uniform tidal heating by mean flows. J. Geophys. Res. 106 (E12), 32971–32981.

Tackley, P.J., 2008. Modelling compressible mantle convection with large viscosity contrasts in a three-dimensional spherical shell using the yin-yang grid. Phys. Earth Planet. Interiors 171, 7–18.

Tackley, P.J., Schubert, G., Glatzmaier, G.A., Schenk, P., Ratcliff, J.T., Matas, J.-P., 2001. Three-dimensional simulations of mantle convection in Io. Icarus 149, 79–93.

Turcotte, D.L., Schubert, G., 1982. Geodynamics: Applications of Continuum Physics to Geological Problems. Wiley, New York.

Turtle, E.P. et al., 2001. Mountain on Io: High-resolution Galileo observations, initial interpretations, and formation models. J. Geophys. Res. 106(E12), 33175–33199.

Veeder, G.J., Matson, D.L., Johnson, T.V., Blaney, D.L., Goguen, J.D., 1994. Io's heat flow from infrared radiometry, 1983–1993. J. Geophys. Res. 99, 17095–17162.

Yoder, C.F., Peale, S.J., 1981. The tide of Io. Icarus 47, 1–35.

Zhang, H., Zhang, C.-Z., 2001. The figure and dynamical parameters of Io inferred from internal structure models. Chin. J. Astron. Astrophys. 1 (3), 275–280.